

Design and Testing of Subsystems for Mo-99 Production

Nuclear Engineering Division

About Argonne National Laboratory

Argonne is a U.S. Department of Energy laboratory managed by UChicago Argonne, LLC under contract DE-AC02-06CH11357. The Laboratory's main facility is outside Chicago, at 9700 South Cass Avenue, Argonne, Illinois 60439. For information about Argonne and its pioneering science and technology programs, see www.anl.gov.

DOCUMENT AVAILABILITY

Online Access: U.S. Department of Energy (DOE) reports produced after 1991 and a growing number of pre-1991 documents are available free via DOE's SciTech Connect (<http://www.osti.gov/scitech/>).

Reports not in digital format may be purchased by the public from the National Technical Information Service (NTIS):

U.S. Department of Commerce
National Technical Information Service
5301 Shawnee Road
Alexandria, VA 22312
www.ntis.gov
Phone: (800) 553-NTIS (6847) or (703) 605-6000
Fax: (703) 605-6900
Email: **orders@ntis.gov**

Reports not in digital format are available to DOE and DOE contractors from:

U.S. Department of Energy
Office of Scientific and Technical Information
P.O. Box 62
Oak Ridge, TN 37831-0062

Disclaimer

This report was prepared as an account of work sponsored by an agency of the United States Government. Neither the United States Government nor any agency thereof, nor UChicago Argonne, LLC, nor any of their employees or officers, makes any warranty, express or implied, or assumes any legal liability or responsibility for the accuracy, completeness, or usefulness of any information, apparatus, product, or process disclosed, or represents that its use would not infringe privately owned rights. Reference herein to any specific commercial product, process, or service by trade name, trademark, manufacturer, or otherwise, does not necessarily constitute or imply its endorsement, recommendation, or favoring by the United States Government or any agency thereof. The views and opinions of document authors expressed herein do not necessarily state or reflect those of the United States Government or any agency thereof, Argonne National Laboratory, or UChicago Argonne, LLC.

Design and Testing of Subsystems for Mo-99 Production

by

R. Gromov, J. Bailey, M. Virgo, S. Chemerisov, and G.F. Vandegrift
Nuclear Engineering Division, Argonne National Laboratory

September 2017

CONTENTS

ABSTRACT	1
1 INTRODUCTION	1
2 DESIGN AND TESTING OF AN ACHROMATIC BENDING BEAMLINE FOR TARGET IRRADIATION	3
2.1 Background	3
2.2 Beamline Design	3
2.3 Implementation	5
2.4 Commissioning and Testing	7
3 DESIGN AND TESTING OF HIGH POWER BEAM DUMP AND COLLIMATOR	9
3.1 Mechanical Design Description and Analyses	9
3.1.1 Beam-Stop Design Description	9
3.1.2 Beam Stop Hydraulic Analyses of the Cooling System	10
3.1.2.1 FATHOM Model Description	10
3.1.2.2 Results and Conclusions	11
3.1.3 Beam Stop Thermal Analyses of Attenuation Plates	11
3.1.3.1 Calculation Description	11
3.1.3.2 Calculation Results and Conclusion	12
3.1.4 Beam Stop Thermal-Hydraulic Analyses of the Image Plate	13
3.1.4.1 ANSYS CFX Model Description	13
3.1.4.2 Results and Conclusions	14
3.1.5 Beam Stop Stress Analysis of Image Plate	16
3.1.5.1 Model Description	16
3.1.5.2 Results and Conclusion	16
3.1.6 Collimator Design	17
3.1.7 Hydraulic Analyses of the Collimator Cooling System	18
3.1.8 Thermal-Hydraulic Analyses of Collimator Front Section	19
3.1.8.1 ANSYS CFX Model Description	19
3.1.8.2 Results and Conclusions	20
3.2 Installation and Testing of Beam Dump and Collimator	20
3.2.1 Installation	20
3.2.2 Experimental Results	22
3.2.3 Conclusion	27
4 OVERALL SUMMARY AND CONCLUSIONS	28
5 REFERENCES	29
APPENDIX 1	31

FIGURES

1	Relationship between the physical center of the first 10° bend and the corresponding beam trajectory.....	4
2	Simulated horizontal and vertical beam envelopes for the achromatic bend assuming an energy spread of $\pm 2\%$	5
3	Schematic showing the +20° beamline.....	6
4	Photograph of the installed beamline showing the tables, alignment stages, and magnets.	7
5	Energy spectrum of the beam used for testing.....	8
6	Beam distribution with horizontal and vertical intensity profiles taken through the approximate center of the beam.	8
7	Design of beam stop assembly.....	9
8	Design of beam stop FATHOM hydraulic model.....	10
9	Internal heat generation in aluminum beam stop due to 40 MeV beam impingement.	12
10	Boiling criteria in cooling channels for different plate thicknesses and beam sizes.	13
11	Front plate design.....	14
12	Results of CFX thermal hydraulic analysis for flow velocity in channel, pressure across channel, temperature of channel wall, and temperature of aluminum plate	15
13	ANSYS structural model of image plate	16
14	ANSYS stress results for image plate.....	16
15	Collimator assembly drawings.....	17
16	Collimator attenuator with cooling channels.	18
17	Collimator FATHOM hydraulic model.	19
18	ANSYS CFX thermal hydraulic results for collimator.....	20
19	Experiment setup. 1 – Beam dump, 2 – Collimator, 3 – OTR-camera holder, and 4 – Quads.....	21

20	OTR-camera technical drawings. 1 – Bottom plate, 2 – OTR-camera, 3 – Small-angle optic, 4 – Protective holder, 5 – Adjustable mirror holder with aluminum elliptical mirror.	22
21	Input and output cooling water temperature for collimator with 6 kW of beam average power.	23
22	Target interlock protection logic.....	24
23	Collimator current with low repetition rate.	24
24	Beam-dump thermocouple temperature vs. time measurements: (a) 44 x 40 mm, 20 kW beam, (b) 30 x 30 mm, 15 kW beam, and (c) 20 x 20 mm, 10 kW beam.	25
25	Beam dump front plate surface at the OTR camera.....	26
26	Defocused electron beam at the front plate of the beam dump.....	26

This page intentionally left blank

DESIGN AND TESTING OF SUBSYSTEMS FOR MO-99 PRODUCTION

R. Gromov, J. Bailey, M. Virgo, S. Chemerisov, and G. F. Vandegrift

ABSTRACT

Argonne National Laboratory, in cooperation with Los Alamos National Laboratory, is developing technology with NorthStar Medical Technologies to produce ^{99}Mo from the γ, n reaction on a ^{100}Mo target in an electron accelerator. During production runs and thermal testing of the helium-cooled target, it became obvious that a production-scale beam-line configuration would need a collimator to protect the target from accidental beam misplacement or a beam-profile change. A prototype high-power collimator and beam stop were designed and fabricated. Testing indicated that they will be able to operate at full power in the production-scale accelerator.

1 INTRODUCTION

An electron accelerator can be used to produce ^{99}Mo from the γ, n reaction on a ^{100}Mo target. With funding provided by the National Nuclear Security Administration's Material Management and Minimization Program, Argonne National Laboratory (Argonne), in cooperation with Los Alamos National Laboratory (LANL), is developing technology with NorthStar Medical Technologies to produce ^{99}Mo by this reaction.

As discussed in previous publications [1, 2], the highest ^{99}Mo yield per gram of ^{100}Mo is achieved by simultaneously irradiating the target from two opposite sides. Beamlines provide the means to deliver the beam to the target. Most of the heat deposition in the target occurs from the slowing down of the electrons, which generates bremsstrahlung photons that, in turn, interact with the ^{100}Mo nucleus to knock out a neutron, thus generating ^{99}Mo . By irradiating from both sides, production of ^{99}Mo is distributed more evenly throughout the target. Because the front window of the target has high-pressure helium on one side and a vacuum on the other side, as well as significant heat deposition from slowing down the electrons in the beam, this window is the most stressed component of the target assembly. By irradiating the target from two sides, one can double the production of the ^{99}Mo isotope while keeping the same thermal load/stress on the target window.

Because the target will be irradiated from two sides by separate accelerators, one would want to eliminate the line-of-sight for the two beams, so that each accelerator does not receive a large radiation dose from the opposing accelerator. This arrangement can be achieved by bending the electron beams with a magnet or with a group of magnets. Any accelerator produces a beam

with a finite energy spread. When going through the magnet, a non-mono-energetic beam will disperse. To avoid this dispersion, one could use an achromatic (non-dispersing) bending system.

The earlier mentioned line-of-sight problem with the two accelerators would activate accelerator components and cause premature failure. To avoid this situation, one could bend the beam so that the bremsstrahlung photons would not hit the opposing accelerator. Because any accelerator will produce an electron beam with some energy spread as well as with beam-energy instability, these bending-magnet systems must deliver a beam with different energies to the same position on the target. Multiple configurations of the bending-magnet systems can accomplish this goal. The design of the system depends on the choice of the accelerator for the production facility. So far, two accelerators have been considered by NorthStar: a linac from MEVEX Corporation and a pulsed Rhodotron[®] from IBA. Those two accelerators have different beam parameters (emittance, energy spread, etc.), which will affect the design of the bending magnet system. In studies to date, we have been using beam parameters for the linac because we have significant operational experience with this accelerator. Based on our experience, a first-order dispersionless bend is considered sufficient for the application of target bombardment.

A beam dump that is capable of accommodating a full-power beam is desired during the initial commissioning, tune-up, and maintenance activities. It is also necessary to obtain the beam-intensity distribution at nominal beam power. In high energy accelerators, where the average current is small, optical transition radiation (OTR) screens are typically used for beam visualization. This would be impossible for a production accelerator because of its very high power. The only possibility for beam visualization in a production facility accelerator setting would be to image the beam on the target or high-power beam dump. A high-power beam dump capable of imaging a full power beam was designed at Argonne and is described in this report.

During production runs and thermal testing of the helium-cooled 12-mm target conducted at Argonne [3–5], it became obvious that a production-scale beam-line configuration would need a collimator to protect the target from accidental beam misplacement or a beam-profile change. The prototype of a high-power collimator was designed and fabricated at Argonne. The design and operating parameters of the beam collimator are discussed in this report.

2 DESIGN AND TESTING OF AN ACHROMATIC BENDING BEAMLINE FOR TARGET IRRADIATION

2.1 BACKGROUND

The collaborative Argonne-LANL effort to develop technologies in support of NorthStar becoming a domestic producer of the ^{99}Mo medical isotope includes both molybdenum disc irradiations and other complementary tasks, such as accelerator component development. Until last year, the accelerator facility at Argonne had two beamlines, one dedicated to NorthStar experiments and the second to subcritical-solution-target-related experiments for producing ^{99}Mo . Irradiations for NorthStar production and thermal experiments using the LANL-designed target are conducted at a fixed target station. Conducting activities that were not performed at the end-target station required uninstalling the beamline leading to the target, assembling the experiment, disassembling the experiment, and reinstalling the beamline. To address this interference, a third beamline was added as a location to carry out non-Mo-target-related tasks. The newly added beamline is described below.

In the previous configuration, a beamline entering the experimental area (“Cell One”) could be sent straight ahead to the NorthStar target or deflected 10° clockwise toward the solution target. These beamlines are referred to as the “zero degree” and “ -10° degree” beamlines, respectively. The vacuum chamber at the nexus of the beamlines had been made with a port oriented at 10° counterclockwise, so there was already a plan to assemble the new beamline in that location.

When bending a beam, a magnet deflects electrons with different energies by different angles. Radio-frequency (RF) accelerators accelerate bunches of electrons to nearly, but not exactly, the same energy. To have control over the final spot size and maintain pulse-to-pulse stability, this dispersive effect must be managed.

2.2 BEAMLINE DESIGN

For this project, we followed the typical approach [6] for achieving achromatic transport, namely, employing a symmetric system whereby dispersion added to the beam in the first dipole is removed in the second. We used what would probably be considered the simplest such configuration, in which a single quadrupole is centered between the two dipoles. When the incoming beam is focused to a waist at the center of the quadrupole, the quadrupole can be adjusted so that the dispersion is canceled while the other properties of the beam remain unchanged. At the exit of the second dipole, the beam returns to the state it was in at the entrance of the first dipole. Because the second dipole is identical to the first, the total bend angle is twice that of either magnet. In this case, the total bend is therefore 20° , and we refer to the new beamline as the “ $+20^\circ$ beamline.”

In the design, the location of the central quadrupole was constrained by the spacing between the 10° section of the new beamline and the existing zero-degree beamline. To avoid interference between the vacuum chamber of the zero-degree beamline and the yoke of the quadrupole, a center-to-center distance of 0.86 m between the two magnets was required. To make the system as compact as possible, this minimum distance was used.

Because the first dipole was used to bend the beam to both the right and the left, its entrance edge was oriented normal to the incoming beam. For symmetry, the exit edge of the second dipole was oriented normal to the outgoing beam. Consequently, the exit edge angle of the first dipole and the entrance edge of the second dipole are 10° . The relationship between the mechanical center of the dipoles and the beam path is illustrated in FIGURE 1. The radius ρ was chosen to be 90 cm.

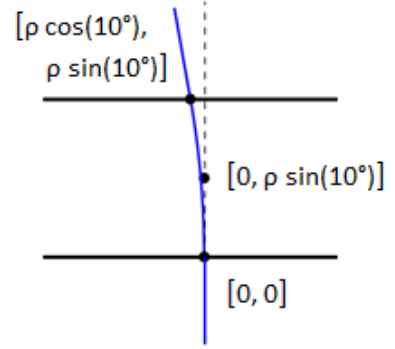


FIGURE 1 Relationship between the physical center of the first 10° bend and the corresponding beam trajectory (ρ is the bend radius). For the second dipole, the orientation is reflected top to bottom.

Given the above dimensions, the distance from the exit edge of the first dipole to the entrance edge of the second dipole is calculated to be 1.48 m. The condition for achromaticity is that the quadrupole centered between the dipoles is set such that the derivative of the dispersion function ($d'_x = R_{26}$) in the radial transfer matrix from the entrance of the first dipole to the center of the system is zero. In the thin lens approximation, this condition is achieved when the focal length f of the quadrupole is $f = .5 d_x / d'_x$. For this configuration, we have $d_x = 0.14$ m and $d'_x = 0.17$, so we get $f = 0.41$ m. The precise field profile of the quadrupole is not known, so we approximate its magnetic length by its physical length, which is $l = 10$ cm. The required quadrupole strength is thus $k \approx 1/\sqrt{fl} = 4.95 \text{ m}^{-1}$. This result can be optimized slightly to account for the finite length of the quadrupole. By numerically multiplying the first-order matrices for the complete system, we found that $k = 4.9 \text{ m}^{-1}$ results in $d_x = 1.4 \times 10^{-3}$ m and $d'_x = 1.5 \times 10^{-3}$ for the transfer matrix between the entrance and exit of the system, showing that the dispersion is effectively canceled.

Considering a beam energy of 40 MeV (Lorentz factor $\gamma = 79$, magnetic rigidity $B\rho = 0.14 \text{ T m}$) as an example, the field required for a bend of radius 90 cm is 1.5 kG, which is well within the capability of the dipoles that have been used. The required quadrupole gradient is $g = B\rho k^2 = 325 \text{ G/cm}$, which is also achievable for the quadrupole.

To preserve the symmetry required for achromaticity, the radial envelope beam must be focused to a waist at the center of the system. There is some flexibility in choosing the waist size, but we can consider an example. We again assume the beam energy to be 40 MeV. We take the normalized emittance (defined in the conventional way as the area of the trace space ellipse divided by π , multiplied by $\beta\gamma$, where $\beta = v/c$ and c is the speed of light in vacuum) to be $200 \text{ } \mu\text{m}$, which is similar to the beam emittance at the Argonne linac. If the beam starts at the center of the system as an upright ellipse with the Courant-Snyder parameters $\hat{\beta}_x = 0.22 \text{ m}$, $\hat{\alpha}_x = 0$, $\hat{\gamma}_x = 4.5 \text{ m}^{-1}$, it exits the system with $\hat{\beta}_x = 3.8 \text{ m}$, $\hat{\alpha}_x = 4.0$, $\hat{\gamma}_x = 4.4 \text{ m}^{-1}$. The ellipse

parameters at the entrance must be equal to the ellipse parameters at the exit, but with the sign of $\hat{\alpha}$ reversed. There is more latitude in setting the characteristics of the axial beam envelope. Because the beam is not dispersed in this orientation, asymmetry about the midplane does not induce first-order dispersion effects. In this example though, we illustrate a symmetric solution with $\hat{\beta}_y = 4.8$ m, $\hat{\alpha}_y = 2.5$, $\hat{\gamma}_y = 1.5$ m⁻¹. Parmela [7] simulation results for the radial and axial beam envelopes using these initial conditions are shown in FIGURE 2. Here, the energy spread is taken to be $\pm 2\%$, which is consistent with the properties of the beam used for the testing.

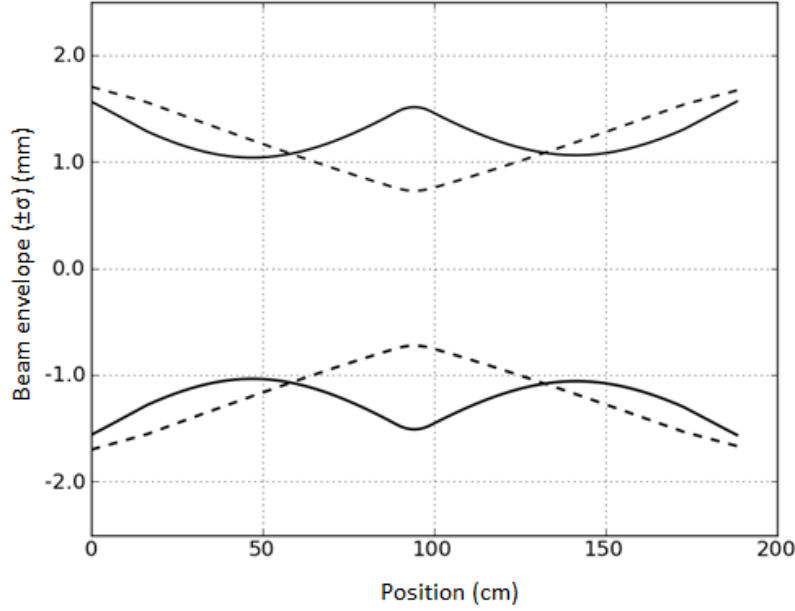


FIGURE 2 Simulated horizontal (solid) and vertical (dashed) beam envelopes for the achromatic bend assuming an energy spread of $\pm 2\%$.

2.3 IMPLEMENTATION

The primary goals for the implementation were (1) simplicity of components and installation, (2) minimization of modifications to the existing configuration, and (3) simplicity of operation.

Two new dipole magnets were purchased from RadiaBeam Technologies, LLC [8]. These square edged dipoles have a gap of 4 cm, a good field width specified to exceed 6 cm, and an effective length of 15.6 cm. Based on measurements made at the vendor's location, the field was linear to just over 2.5 kG (average field). Because the new dipoles were shorter than the existing ones, it was possible to keep the existing components (a steering magnet, aperture, current transformer, and quadrupole doublet) installed between the wall and the first dipole. The additional space was used to add a pneumatically actuated screen for viewing the beam spot. An existing quadrupole was used at the center of the bend. This magnet has a 5.1 cm bore, and the length of the poles is 10 cm. A second diagnostic screen was added on the zero-degree beamline

downstream of the first dipole. Using this second screen in combination with the first one makes it possible to set the position and angle of the beam as it enters the bend. Also, the second screen can be used to help focus the beam to a waist at the center point between the dipoles. On the new beamline, the quadrupole is followed by the second dipole, which is in turn followed by additional diagnostics. Finally, a quadrupole pair is used to focus the beam onto the target. The locations of the beamline elements are shown in FIGURE 3.

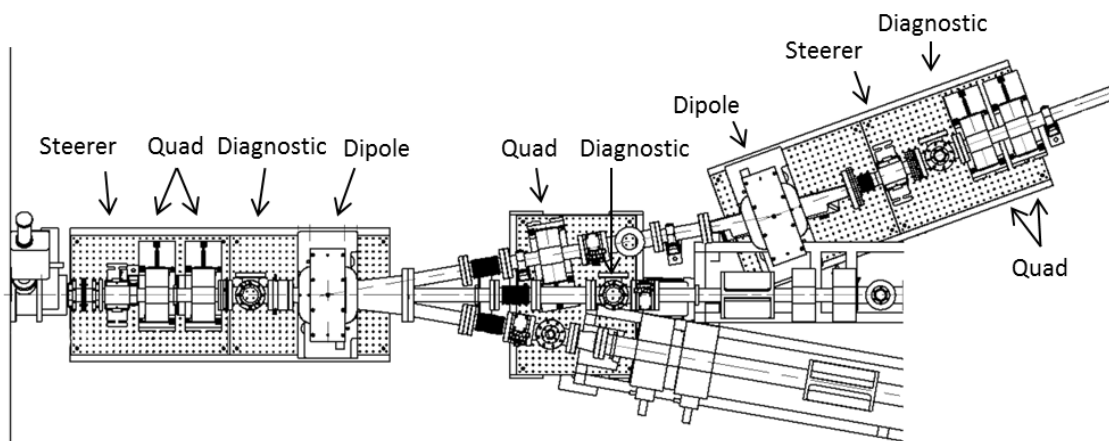


FIGURE 3 Schematic showing the $+20^\circ$ beamline. Also shown are segments of the zero degree and -10° beamlines.

The beamline components were mounted on a series of three aluminum tables topped by optical breadboards. Surveyors were contracted to carry out the final alignment using a laser tracker. Six-axis alignment stages, adapted from designs used at the Stanford Linear Accelerator Center (SLAC), Argonne, and other accelerator labs, were used to accurately position the components at their design locations. The new dipoles were fiducialized to the mechanical structures of the magnets by the manufacturer. The quadrupoles were aligned using the edges of the yokes as a reference. The diagnostic screens were aligned relative to a set of drift nests glued to the positioning stages using optical methods and a coordinate measuring machine (CMM). The surveyors created a reference coordinate system using a combination of features on the existing beamline and optical targets placed during previous surveying activities. Using the laser tracker, positions could be measured with an error of less than $40\text{ }\mu\text{m}$. Typical position errors for the as-located hardware were less than $120\text{ }\mu\text{m}$. A picture of the installed beamline is shown in FIGURE 4.

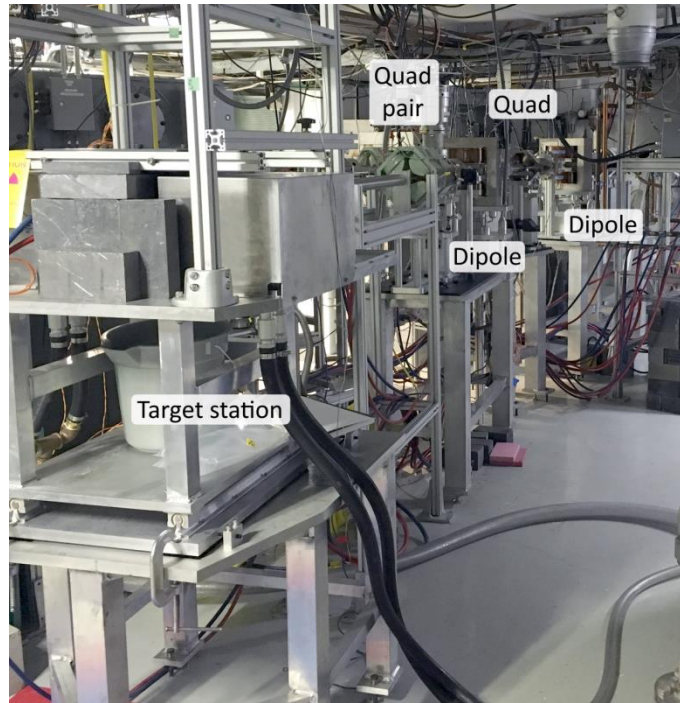


FIGURE 4 Photograph of the installed beamline showing the tables, alignment stages, and magnets. Three vacuum crosses distributed across the length of the beamline house pneumatically actuated screens used to view the beam.

2.4 COMMISSIONING AND TESTING

The beamline was commissioned in December 2016 with a nominal beam energy of 40 MeV.

The beam transport efficiency through the line was about 94% (accelerated pulse current of 0.48 A and current at the exit of the beam line of 0.45 A). The beam energy was approximately 40.0 ± 0.8 MeV full width at half maximum (FWHM). Because the existing spectrometer supports a maximum beam energy of 40 MeV, the beam energy profile was measured in a slightly lower region. The energy profile is shown in FIGURE 5.

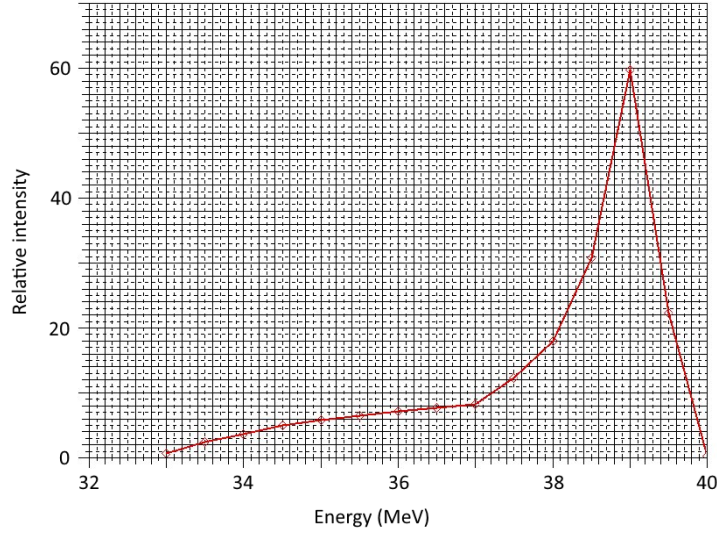


FIGURE 5 Energy spectrum of the beam used for testing. The FWHM energy spread is approximately ± 0.8 MeV.

The transverse profile of the beam at the exit of the beamline was also characterized. It was shown that a compact, symmetrical distribution could be obtained. The distribution, shown in Figure 6, is well-suited for the experiments that will be conducted there.

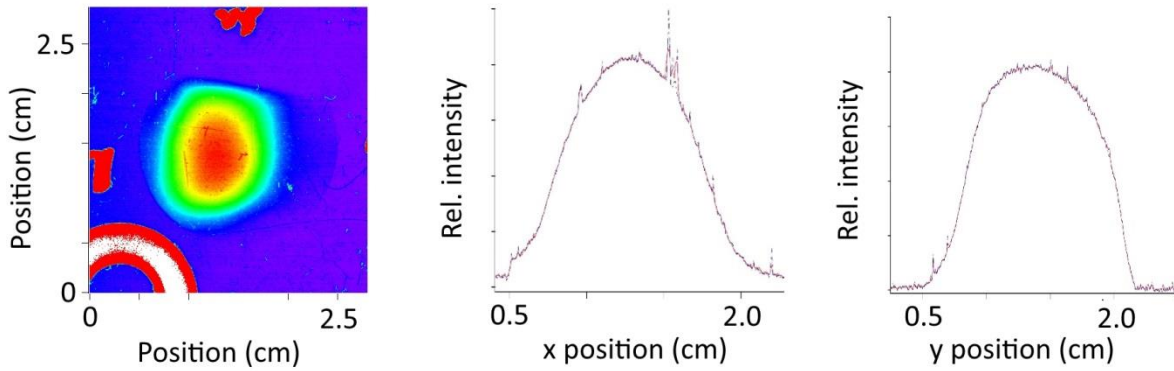


FIGURE 6 Beam distribution with horizontal and vertical intensity profiles taken through the approximate center of the beam. The ring-shaped feature in the lower left is an artifact of the method used to determine the baseline of the distribution.

3 DESIGN AND TESTING OF HIGH POWER BEAM DUMP AND COLLIMATOR

3.1 MECHANICAL DESIGN DESCRIPTION AND ANALYSES

3.1.1 Beam-Stop Design Description

The beam-stop assembly is shown in Figure 7. The assembly consists of a beam line tube, an imaging plate, a series of beam attenuation plates with water channels between them, and a vertical optical port tube. Six thermocouples are embedded in two of the front plates, as shown in Figure 7. The first plate has thermocouples located at the center, 2 in. above center, and 2 in. to one side of center. The second plate has thermocouples located at the center, 2 in. below center, and 2 in. to the other side of center. There is a series-parallel flow arrangement between the plates with inlet and outlet plenums located above and below the plates. Coolant water is supplied and returned to a closed loop heat-exchanger pump system. The beam-line tube is connected directly to the electron beam line and, therefore, is under a vacuum. The imaging plate forms the vacuum boundary at the attenuation plates. The optical port is directly connected to the beam line system and is also under vacuum. The port has a transparent window at the bottom flange for a vacuum seal.

In operation, the horizontal electron beam impinges on the 45° angled imaging plate. The resulting image on the plate is recorded through the image port via a camera mounted outside the transparent window that is below the assembly. The plate stack behind the image plate attenuates the beam and requires water cooling. Temperatures, as read from the embedded thermocouples in the plates, are related to the beam energy deposition and help define the position and shape of the electron beam.

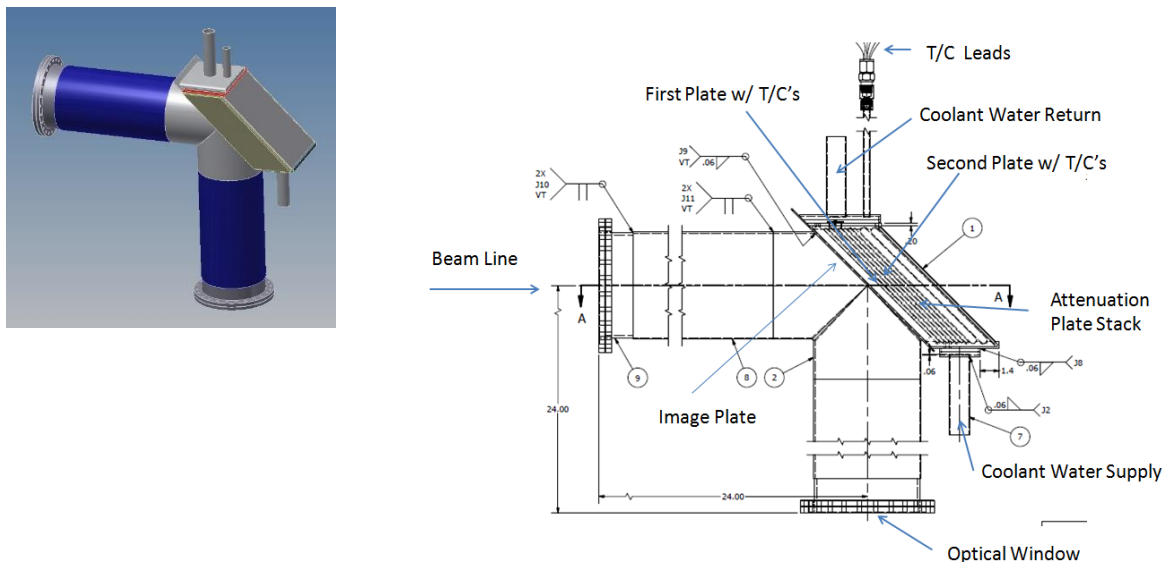


FIGURE 7 Design of beam stop assembly.

then down on the other side of the plate. The leak path around the edges of the plates is indicated on the diagram. The flow from the front and back of the assembly discharges into the common outlet plenum at the top. The total flow is then returned through the header to the cooling system at the bottom.

3.1.2.2 Results and Conclusions

The total flow through the coolant system is 49 gpm (3.1 L/s) with a corresponding pressure loss of 50 psi (0.24 MPa). The average flow velocity in the rectangular flow channels at the front of the assembly is 14.7 ft/sec, and there is an average flow velocity of 11.5 ft/sec in the back channels. Using a classical correlation for flow in a duct and the above flow velocities, the corresponding convective coefficient in the front channels is $1.8 \text{ W/cm}^2\text{-}^\circ\text{C}$, and in the back channels, it is $1.5 \text{ W/cm}^2\text{-}^\circ\text{C}$. These coefficients are used for the following thermal analysis of the plates.

3.1.3 Beam Stop Thermal Analyses of Attenuation Plates

3.1.3.1 Calculation Description

A computer simulation for power deposition and absorption in the aluminum plates versus thickness was performed. For this investigation, the electron beam was assumed to be a Gaussian profile, with FWHM of 50 mm and a total average power of 120 kW. These simulations were performed with the MCNP6 (Monte-Carlo N-Particle) code. According to the results (Figure 9), the highest energy deposition in the beam stop is in the front attenuation plates at the center with a peak power deposition of 4.5 W/cm^3 per 1 kW of beam power. Based on these results, a single worst-case aluminum plate was evaluated. Due to the thinness of the plate, a 1-D axial heat transfer analysis was performed using classical correlations for conduction and convective heat loss. A convective coefficient of $1.8 \text{ W/cm}^2\text{-}^\circ\text{C}$ as determined by the FATHOM hydraulic analysis was applied to both sides of the plate. The edges were assumed to be insulated.

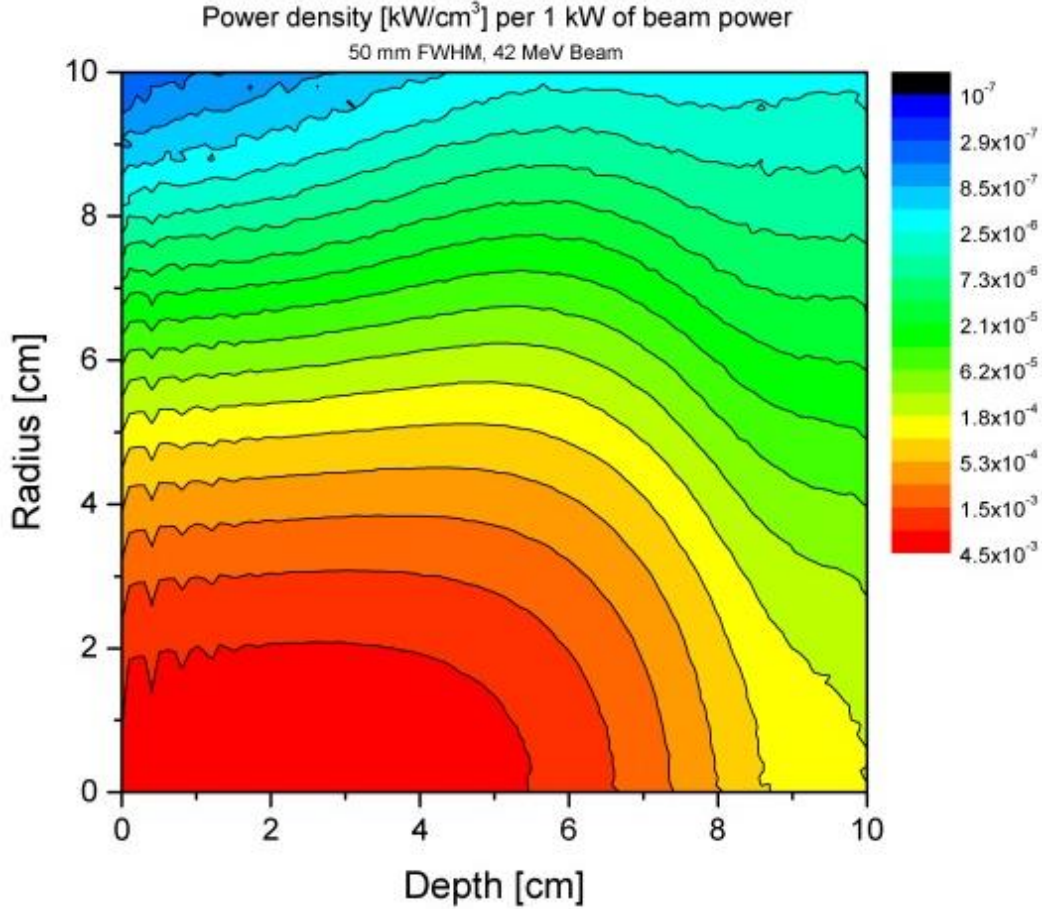


FIGURE 8 Internal heat generation in aluminum beam stop due to 40 MeV beam impingement.

3.1.3.2 Calculation Results and Conclusion

The limiting design criterion for the plate thickness is the avoidance of boiling in the flow channels between the plates (i.e., below 100°C surface temperature). Figure 10 shows plate thickness vs. beam width at 120 kW beam power based on 1-D heat transfer calculations at the center of the plate (i.e., location of maximum heat generation). As indicated by the figure, the maximum allowable plate thickness considering a beam width of 50 mm FWHM is 0.50 cm (0.20 in). Therefore, the design of the front plates utilized a 3/16-in. stock aluminum plate. Also, the maximum temperature at the center of the plate was calculated to be 107°C, which is well within the allowable temperature design limit.

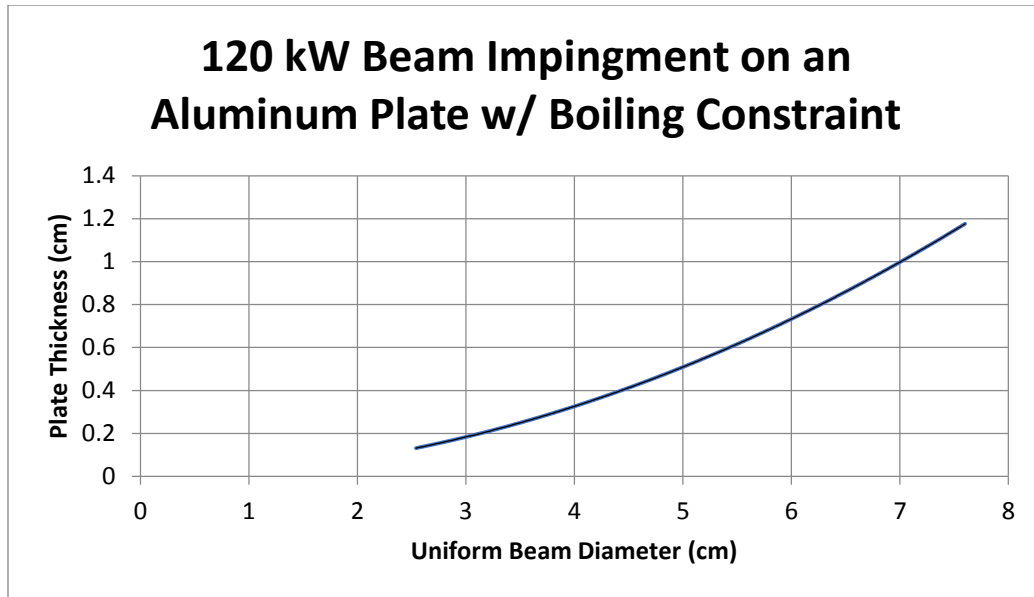


FIGURE 9 Boiling criteria (surface temperature equal to 100°C) in cooling channels for different plate thicknesses and beam sizes.

3.1.4 Beam Stop Thermal-Hydraulic Analyses of the Image Plate

3.1.4.1 ANSYS CFX Model Description

The front plate of the beam stop functions both as an imaging screen and as a boundary between the beam-line vacuum and the coolant flow between the plates. Because of the resulting pressure loading across the plate, reinforcement ribs were required between the imaging plate and the first attenuation plate (Figure 11). Due to the complex geometry, a thermal hydraulic CFX model was required. A half- symmetry model of a flow channel and rib, assumed located at the center of the plate, was developed. The heat deposition as described in the previous section was used as input for this CFX model. The flow conditions at the inlet to the channel were obtained from the previous FATHOM hydraulic analysis. The vacuum side and edges of the plate were assumed to be insulated and to have negligible radiant-heat transfer.

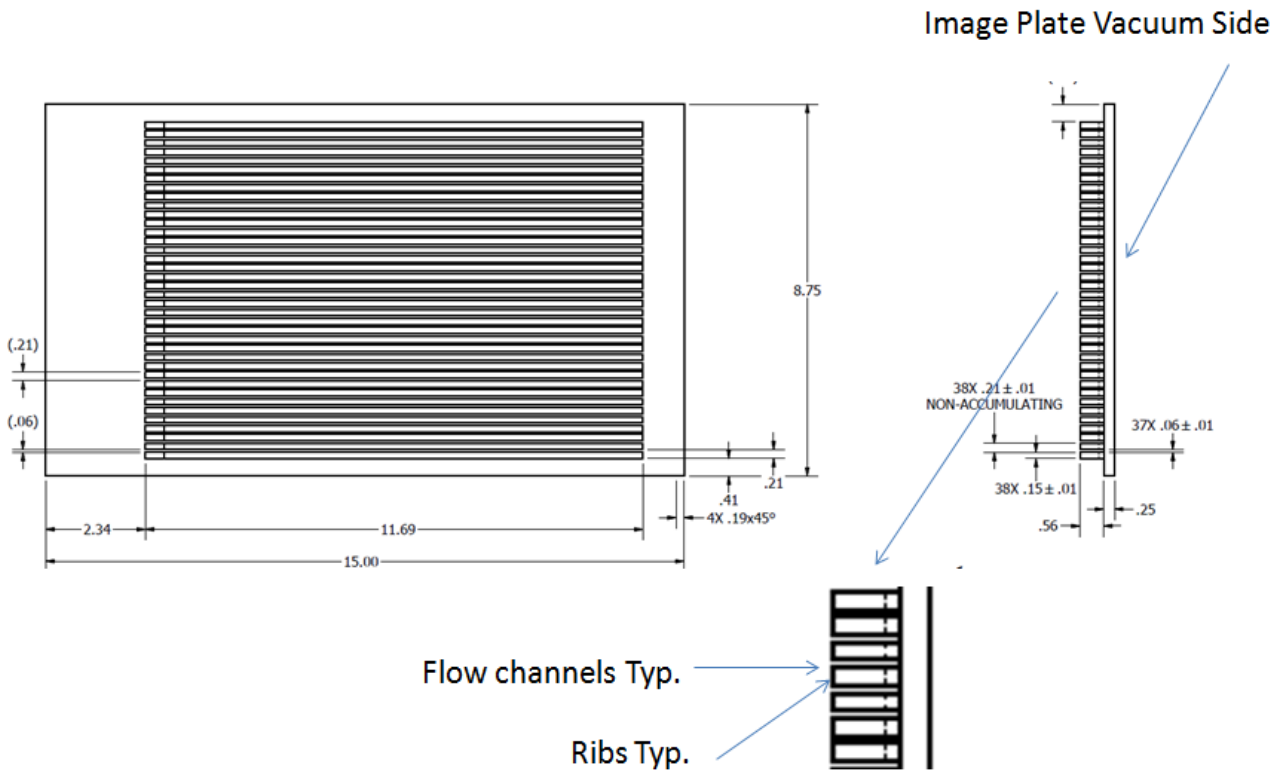
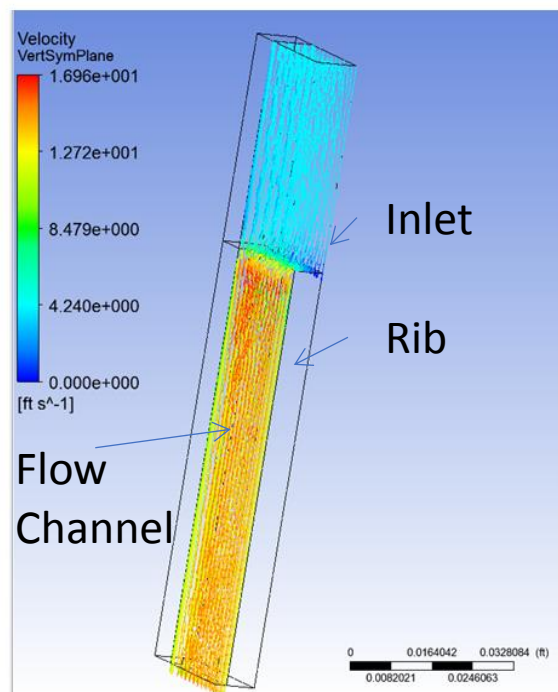


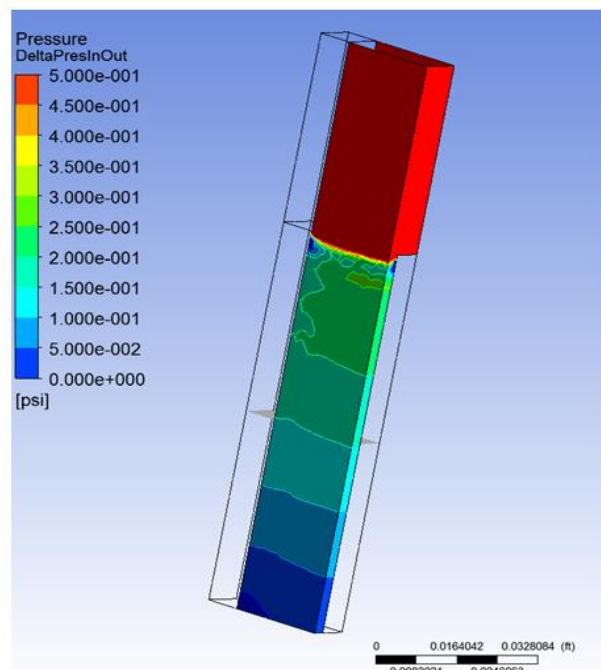
FIGURE 10 Front plate design (units are in inches).

3.1.4.2 Results and Conclusions

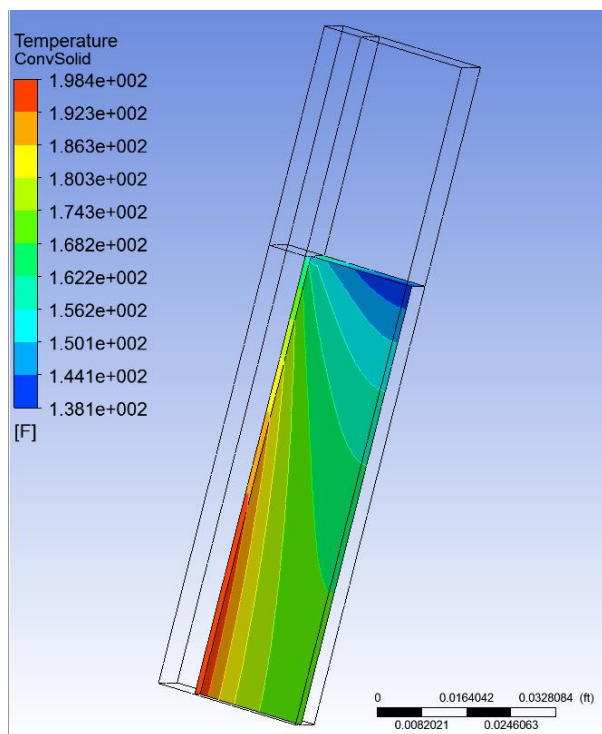
The resulting flow velocities are shown in Figure 12-A. The average flow velocity in the channel is 14 ft/sec (4.3 m/s), which is a practical design value and is consistent with the FATHOM hydraulic analysis describe above. The corresponding pressure profile across the channel is shown in Figure 12-B. These values are also within practical limits and are consistent with the hydraulic analysis, which has an overall pressure loss of 0.5 psi. The resulting thermal analysis showing the surface temperature of the channel walls is shown in Figure 12-C. The maximum wall surface temperature is indicated as 198°F (92°C), which is reasonably below the boiling design criterion of 212°F (100°C). Also, the maximum temperature of 210°F (99°C) in the aluminum plate, as shown in Figure 12-D, is well within the design limits. Based on these thermal hydraulic analyses, the design was determined to be acceptable.



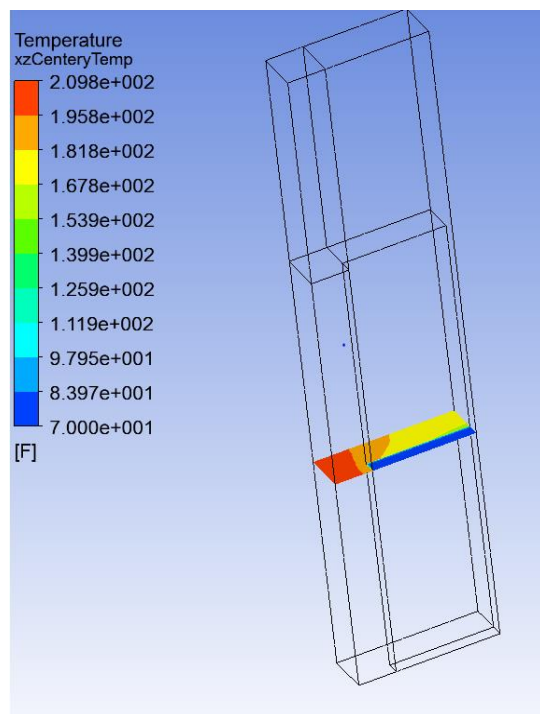
A



B



C



D

FIGURE 11 Results of CFX thermal hydraulic analysis for (A) flow velocity in channel, (B) pressure across channel, (C) temperature of channel wall, and (D) temperature of aluminum plate

3.1.5 Beam Stop Stress Analysis of Image Plate

3.1.5.1 Model Description

Because of the pressure loading across the image plate, a stress analysis was performed using the ANSYS [10] computer code to provide input to the design. The structural analysis model of the image plate is shown in Figure 13. A pressure load of 75 psi (0.52 MPa) relative to the vacuum in the beamline tube is applied. The image plate is constrained by a partial representation of the walls of beamline tube.

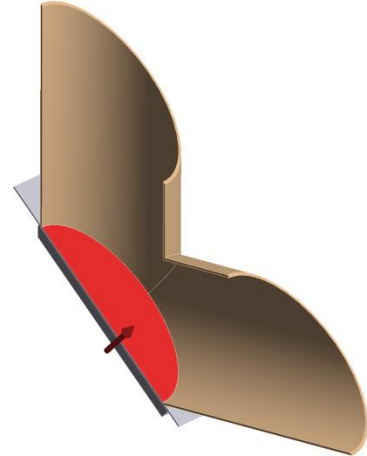


FIGURE 12 ANSYS structural model of image plate

3.1.5.2 Results and Conclusion

The resulting stress intensity is shown on the left in Figure 14. The maximum stress in the image plate is well below the limit of 18 ksi (124 MPa) of the material, as defined in the ASME pressure vessel code Section VIII, Division 2. The peak stress value above 18 ksi is only an artifact of the model due to a geometric discontinuity. The deflection of the image plate is shown to the right of Figure 14.

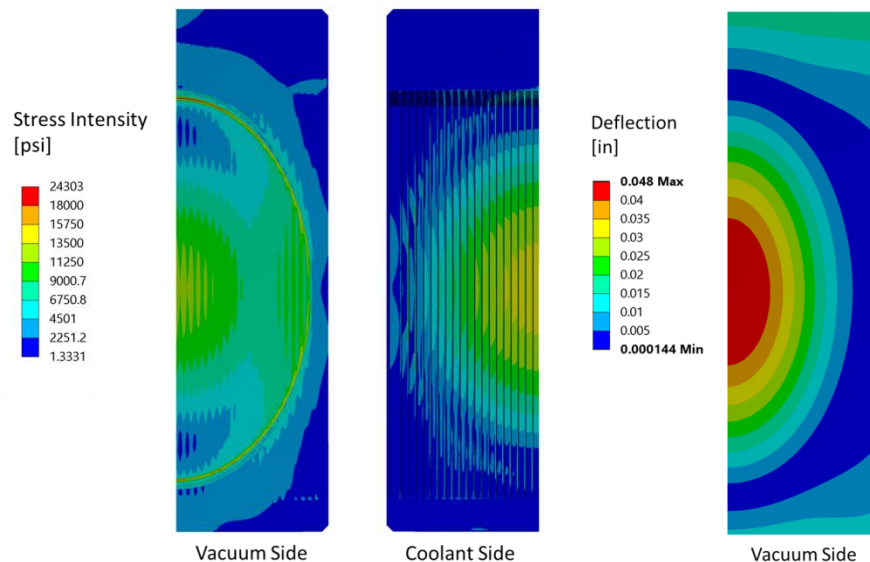


FIGURE 13 ANSYS stress results for image plate

3.1.6 Collimator Design

The design of the collimator is shown in Figure 15. The cylindrical aluminum collimator is installed in the beam tube upstream of the target assembly. The coolant supply and return lines pass through into the beam tube at a flange assembly and are sealed with compression fittings in the flange face. The coolant lines run through the beam-line tube to the front of the collimator where they connect to the collimator coolant channel.

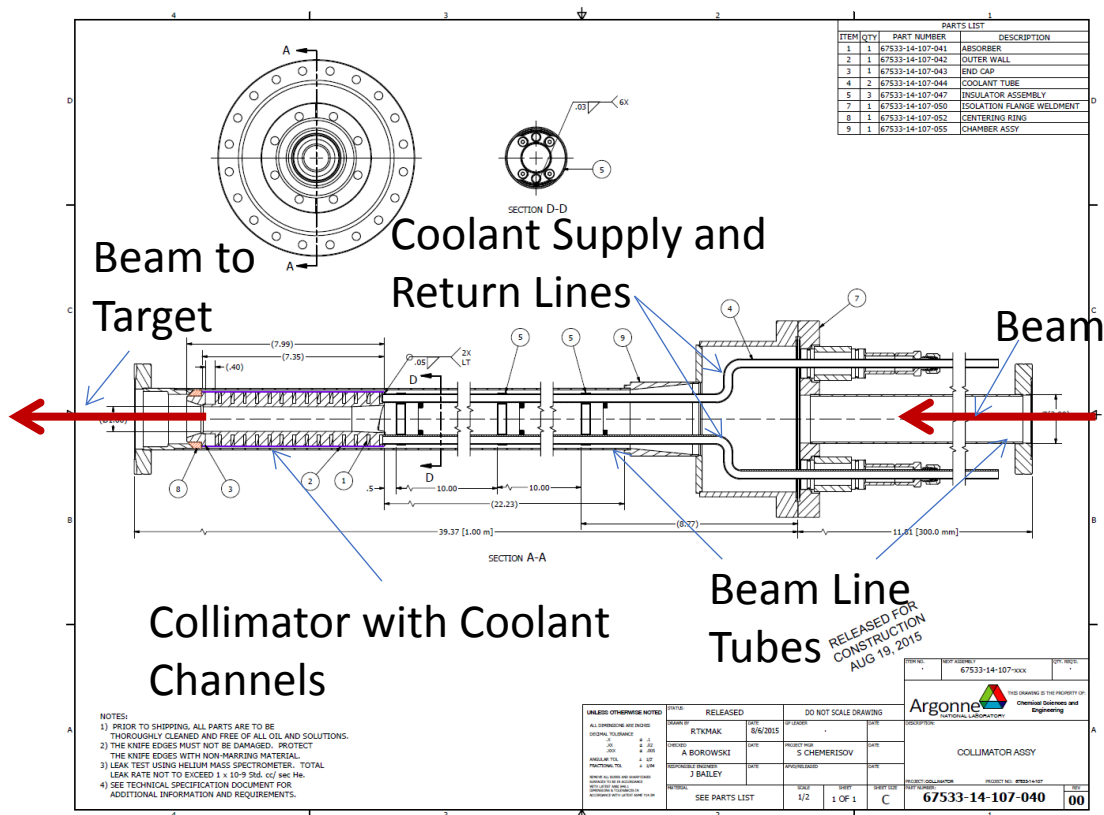


FIGURE 14 Collimator assembly drawings.

As shown in Figure 16, the collimator's coolant channel is a double helix that is cut into the collimator's cylindrical wall. The channel has a rectangular cross section. One of the helix channels is the supply, and the flow is from the front of the collimator through the helix to the back plenum. The flow is then returned from the back plenum through the second helix channel to the front of the collimator, where it is connected to the return tube.

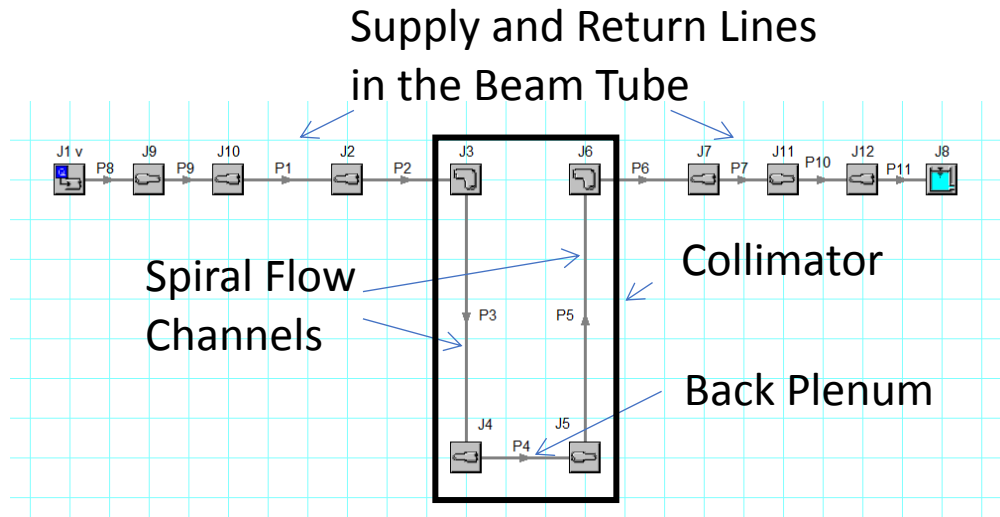


FIGURE 16 Collimator FATHOM hydraulic model.

3.1.8 Thermal-Hydraulic Analyses of Collimator Front Section

3.1.8.1 ANSYS CFX Model Description

The front section of the collimator has the highest internal heat generation from the beam and also has the largest material region between the cooling channels. Therefore, it is considered to be the limiting case for thermal criteria. Two criteria are considered: (1) avoidance of coolant boiling in the channel and (2) maximum allowable temperature for the aluminum body. The CFX model consists of the cylindrical front portion of the collimator that extends from the axial back to half of the first flow channel. A symmetric boundary is assumed for the other half of the flow channel. An axial cross section is shown in Figure 18. The peak heat deposition as described in the previous thermal analysis sections for a 120-kW, 50-mm FWHM electron beam was used as input to this CFX model. The thermal convective coefficient was calculated by using classical correlations for duct flow. Flow velocities were obtained from the previous hydraulic FATHOM analysis. Boundary conditions are as indicated in Figure 18.

Collimator Thermal Results – Cross Section

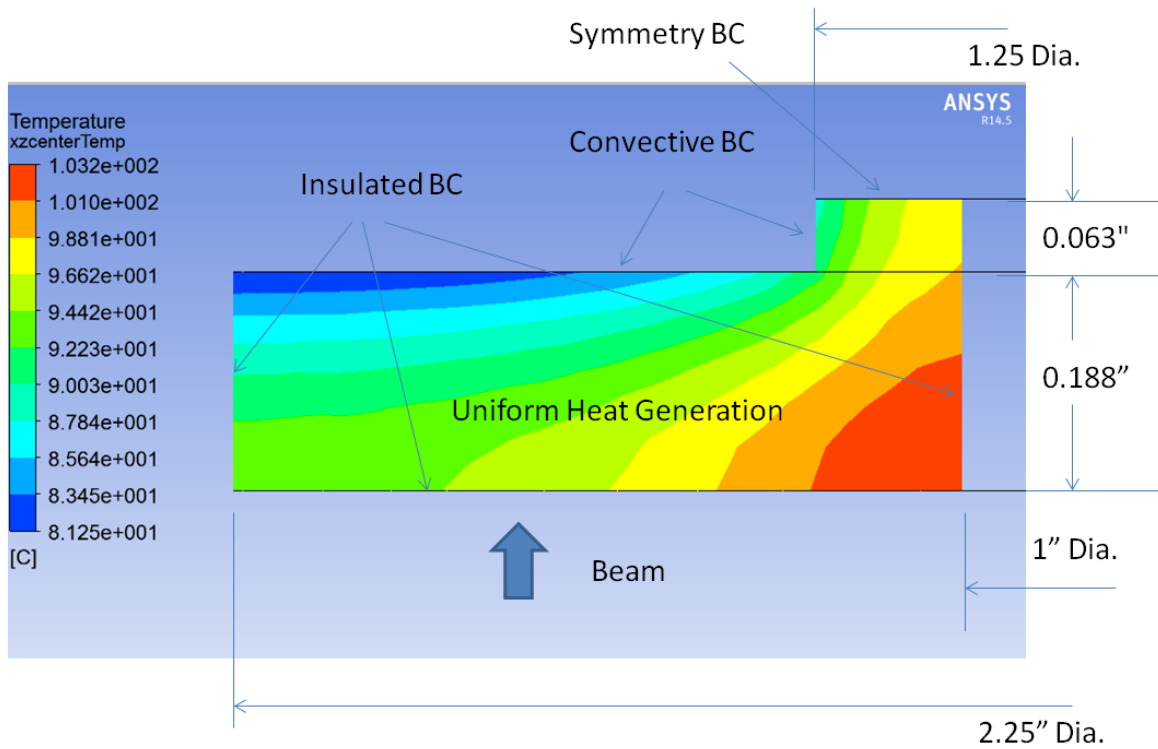


FIGURE 17 ANSYS CFX thermal hydraulic results for collimator.

3.1.8.2 Results and Conclusions

The temperature profile through the axial cross section of the front of the collimator is shown in Figure 18. The walls of the flow channel are indicated by the convective boundary condition. The maximum surface wall temperature of 90°C is seen to be in the corner of the channel. This temperature is significantly below the saturation temperature of the coolant water and, therefore, meets the design criteria. Also, the maximum aluminum temperature, as shown in Figure 18, is 103°C, which is well below the allowable design temperature for the aluminum, and therefore, it meets the design criteria.

3.2 INSTALLATION AND TESTING OF BEAM DUMP AND COLLIMATOR

3.2.1 Installation

Experimental runs with prototypes of the beam dump and collimator were performed at the straight line (zero-degree mark) in the experimental Cell-1 area at Argonne's Low-Energy Accelerator Facility (LEAF) [11]. The maximum average power of the electron beam is about 20 kW, which is sufficiently lower than the design parameters for the beam dump and collimator

(120 kW). After it was assembled, the vacuum chamber was leak checked and pumped down by a turbo pump to 10^{-7} torr.

The beam dump was installed at the end of the beam line (Figure 19). A thermo-stabilized cooling-water line was connected to the beam dump. The water temperature was about 15°C , and the flow rate was about 19 gpm (1.2 L/s). A set of thermocouples was built into the 6th and 9th aluminum plates of the beam dump. Their places are at the center of the beam, with a vertical offset at 5 cm and a horizontal offset at 5 cm. The readings of those thermocouples were recorded by a XL100 Omega data logger.

The collimator was installed just before the beam dump. The cooling water was not thermostabilized; the average water flow was 1.3 gpm (0.08 L/s). The temperature of the incoming and returning water was controlled by LABView monitoring equipment. Because the inner diameter of the collimator was 1 in. (2.5 cm), the installation and test of the collimator were performed after the beam-dump test. This test was made to maximize the power deposition from a defocused electron beam on the beam dump.

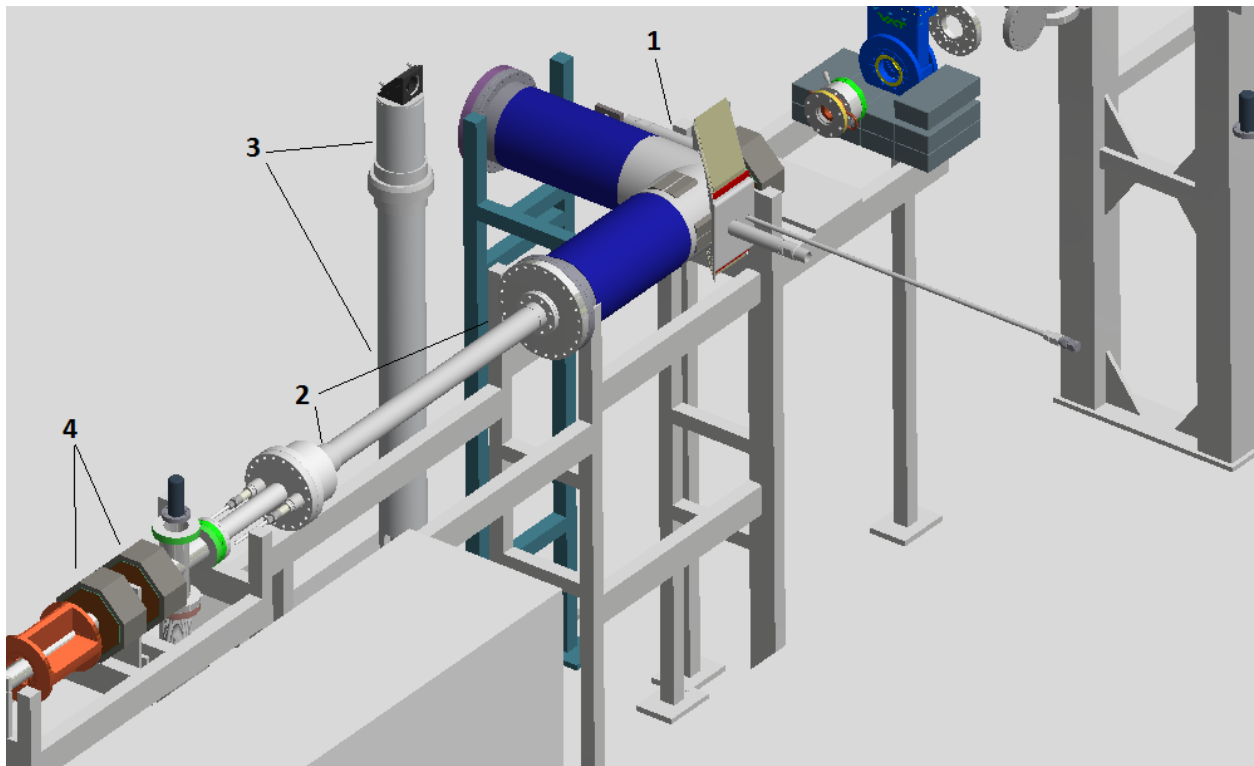


FIGURE 19 Experiment setup. 1 – Beam dump, 2 – Collimator, 3 – OTR-camera holder, and 4 – Quads.

The optical transition radiation (OTR) camera was installed in a special holder (Figure 20) with an aluminum mirror, which helped to align the camera at the face of the front plate of the beam dump and also allowed the installation of lead and borated polyethylene shielding to protect it from excessive gamma radiation and neutron flux. After installation, the scale of the image of the OTR camera was verified by the ruler, and this ratio was used to measure the actual size of the beam spot at the target.

3.2.2 Experimental Results

The first experiments were performed with the collimator and beam dump installed at the end of the transport line. The temperature of the collimator cooling water was logged by in-house designed LABView-based software. The systematical error was high due to the excessive noise sensitivity of the control electronics (Figure 21). Since the collimator was designed to withstand an average power of up to 20 kW of electron beam with an energy of 40–42 MeV, the beam was defocused to increase the power deposition at the collimator and make it more uniform. The beam was defocused at the size 17 x 16 mm FWHM and the maximum average power was 6.0 kW. The cooling-water flow rate was 1.2 gpm (0.076 L/s), and the temperature rise was $dT = T_{OUT} - T_{IN} = 31.4 \pm 0.8 - 27.4 \pm 0.9 = 4.0 \pm 1.2^\circ\text{C}$.

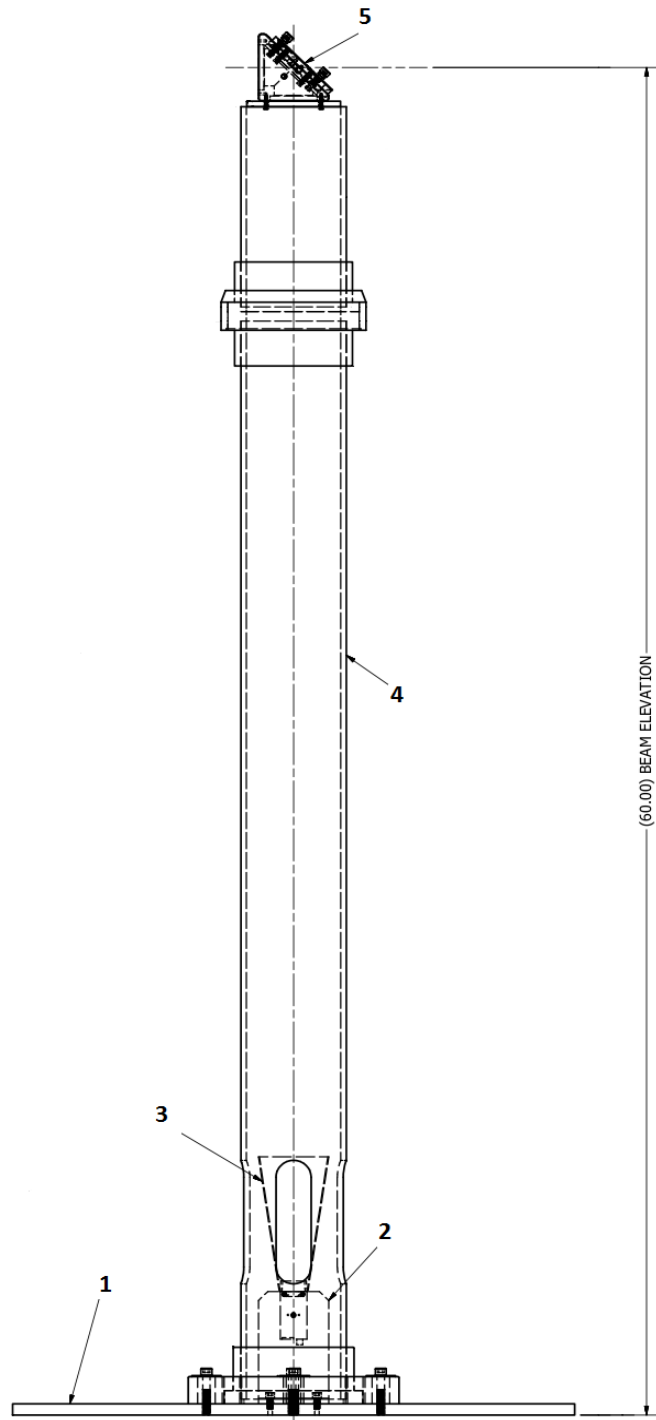


FIGURE 20 OTR-camera technical drawings. 1 – Bottom plate, 2 – OTR-camera, 3 – Small-angle optic, 4 – Protective holder, 5 – Adjustable mirror holder with aluminum elliptical mirror.

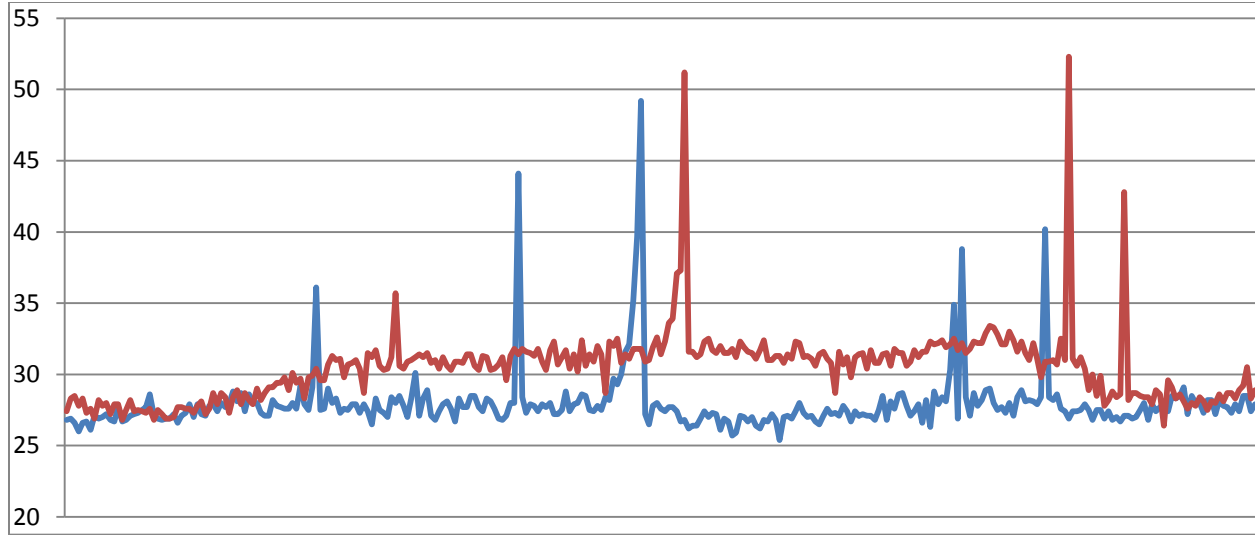


FIGURE 21 Input (blue) and output (red) cooling water temperature for collimator with 6 kW of beam average power.

The collimator body is insulated to ground, so the fraction of the beam, deposited at the collimator, can be estimated by the current reading. This measurement is used to monitor the stability of the beam position at the reference trajectory. The target interlock protection system is based on the collimator current reading. The protection mechanism is implemented in the hardware (Figure 22). If the collimator current exceeds the maximum tripping level, it means the beam has deviated too far from the axis or it has been defocused. If the collimator current drops down to the minimum trip level, one of the following conditions has been encountered: the beam has been completely lost on its way to the target (malfunction of the bending magnet, etc.); the beam has been over focused, resulting in a significant increase in power deposition over a small region on the target; or the collimator connection has been lost. In any of these cases, the high-power electron beam must be tripped immediately. The test of the electronics was performed separately with the reading of the current using a Faraday cup. The tripping of the system occurred in less than 1 μ s, which is sufficient to trip the accelerator running with 800 Hz before the next pulse. Part of the logged data during the beam-size and position-tuning process for the collimator current measurement is presented in Figure 23.

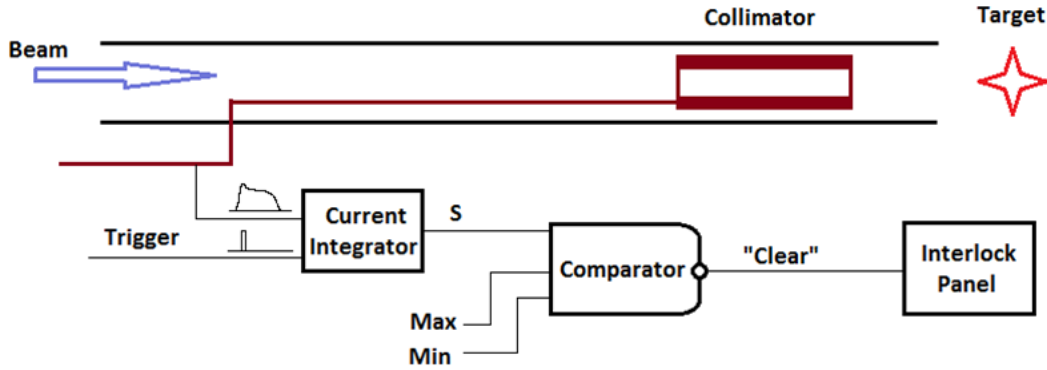


FIGURE 22 Target interlock protection logic.

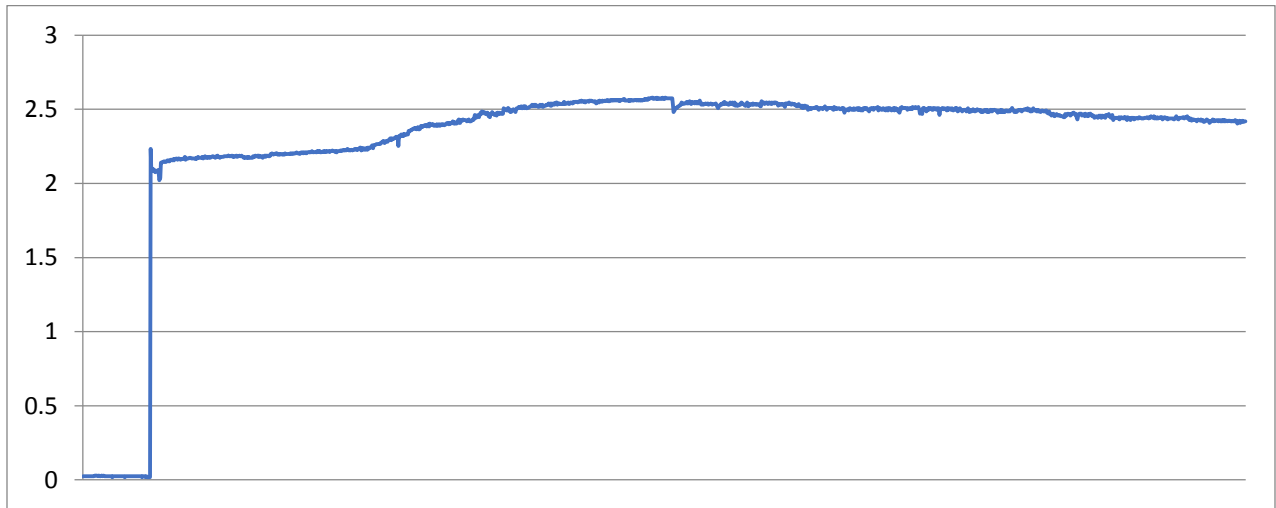


FIGURE 23 Collimator current (in μA) with low repetition rate.

For the next experimental run that was performed, only the beam dump was installed at the end of the beam-transport line. At this step, a nipple was installed at the place of the collimator, and the beam line was pumped down to 10^{-7} torr. The electron beam was defocused to achieve different transverse sizes at the front face of the beam dump. This was done to achieve different energy depositions on the beam dump's volume. The beam size was controlled by a focus/defocus (FODO) quadrupole doublet. An OTR camera was used to monitor the Gaussian transverse profile of the beam at the front face of the beam dump.

Testing runs were performed with the beam transverse size from 20 x 20 mm up to 40 x 44 mm and an average power of up to 20 kW. The average power of an electron beam was restricted by the accelerator power limit (20 kW). The cooling water flow rate was provided by the water cooling pump stand that was limited to 19 gpm (1.2 L/s) due to the limited cross section of the already-installed supply lines. The temperature measurements are presented in Figure 24. The first irradiation was conducted with a 44 x 40 mm beam, and the beam power was

raised in steps to 20 kW. The second irradiation is for a 30 x 30 mm beam and maximum power of 15 kW. The last set of measurements corresponds to a beam size 20 x 20 mm and a maximum average beam power of 10 kW.

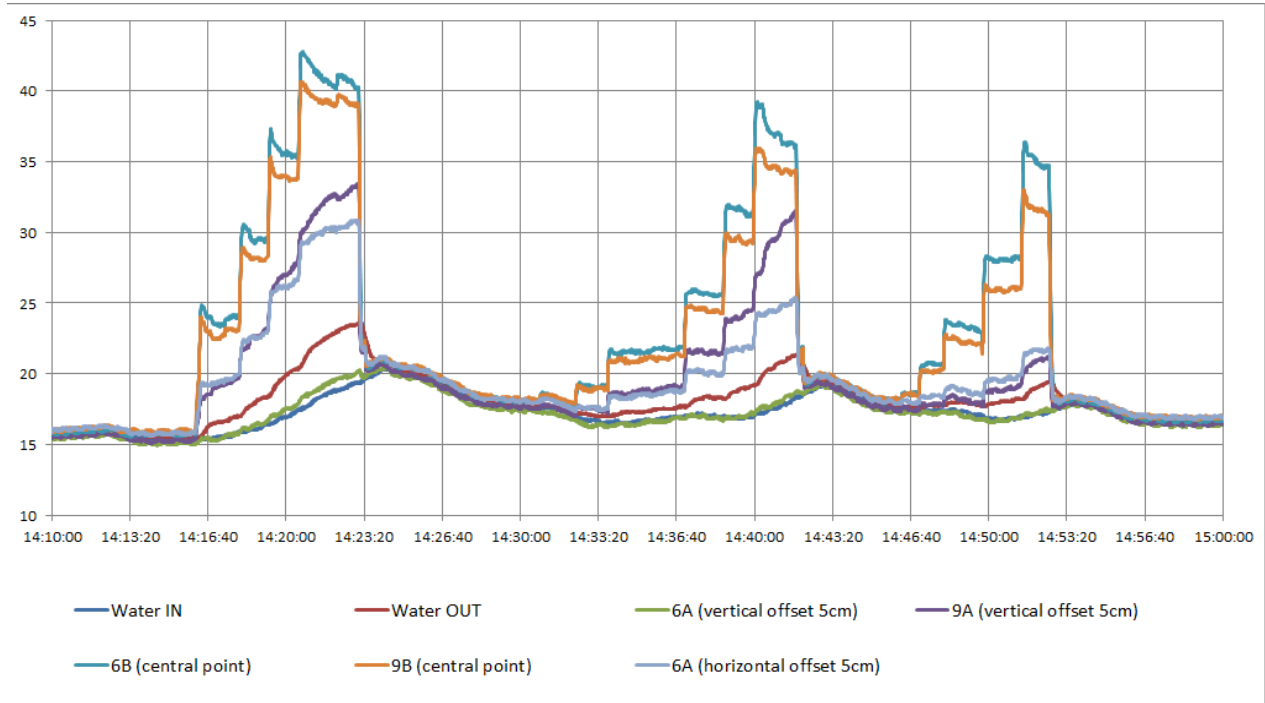


FIGURE 24 Beam-dump thermocouple temperature (°C) vs. time measurements: (a) 44 x 40 mm, 20 kW beam, (b) 30 x 30 mm, 15 kW beam, and (c) 20 x 20 mm, 10 kW beam.

The transverse beam profile at the front plate of the beam dump was monitored by a BASLER OTR camera. The total distance from the camera to the front plate of the beam dump was 178 in. (4.52 m). To calibrate the screen resolution, a reference picture of a ruler at the given distance was made prior of the experimental runs (Figure 25).



FIGURE 25 Beam dump front plate surface at the OTR camera.

The measurement of the beam transverse cross section was performed by software developed by Mike Holloway (LANL). Pictures of the beam spot were logged on the computer hard drive (Figure 26).

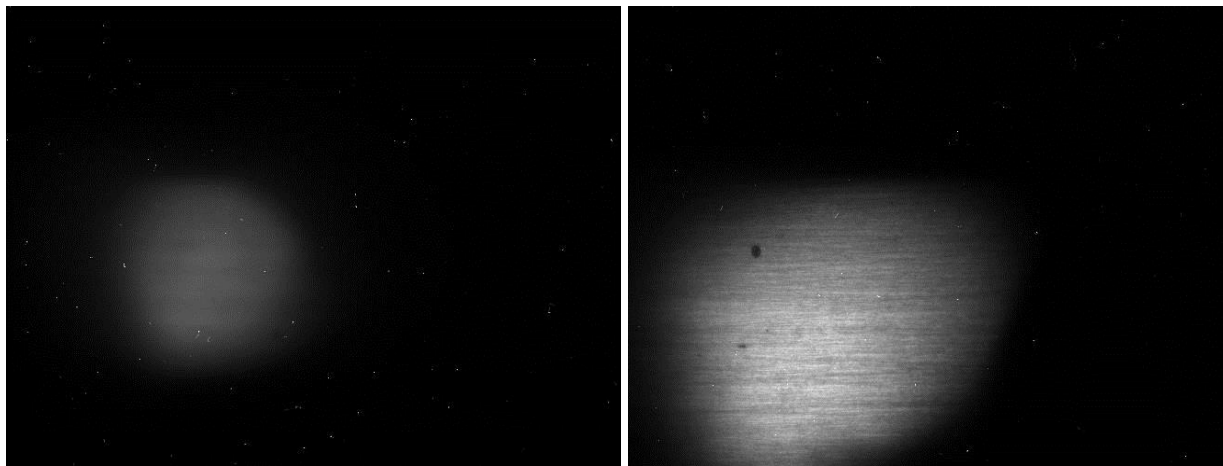


FIGURE 26 Defocused electron beam at the front plate of the beam dump. OTR-camera diaphragm is set to the minimum opening.

3.2.3 Conclusion

Testing of the collimator was performed with a defocused beam of average power 6.0 kW. The beam halo power was dumped by the collimator. The cooling water temperature rise was $4.0 \pm 1.2^\circ\text{C}$. With a water flow of 1.2 gpm (0.076 L/s), this corresponds to about 1.3 kW of power. With a beam size of 17 x 16 mm FWHM and a collimator inner diameter of 25.4 mm, the measured values appear to be reasonable. The design and implementation of this collimator prototype can be used as a basis for the NorthStar collimator.

Based on the linac's ultimate beam parameters (beam energy $E = 40$ MeV, beam-spot size 40 x 44 mm, and average power = 40 kW), the new set of simulations of power distribution was performed for three beam sizes: 20 x 20 mm, 30 x 30 mm, and 42 x 42 mm. The average power was consequently 10 kW, 15 kW, and 20 kW. According to the compliance of the thermocouple measurements to the simulation result, the center of the beam was offset by about 20 mm, and that was not crucial for the beam dump performance. The actual measured temperature for the given flow rate and beam power density was at about 3–5 degrees lower than predicted by the computer simulations. It has been demonstrated that the beam dump simulation and design are reliable and can be used to work with the beam set at the average energy of up to 120 kW.

4 OVERALL SUMMARY AND CONCLUSIONS

To allow accelerator technology development for NorthStar to be carried out without interrupting the progress of Mo-disk irradiations, an additional achromatic beamline section was designed and added to the Argonne linac. To achieve achromaticity, a symmetric bend-quadrupole-bend configuration of beamline elements was employed. A combination of existing and newly purchased components was used to meet the required specifications while limiting the associated costs. The beamline was commissioned at just under 40 MeV, and the beam properties at the target were determined. No significant setbacks were encountered during the commissioning, and the new beamline is now in use.

Subsequently, the collimator and beam-stop designs were tested. The results showed that the beam stop and collimator will be able to operate at full power of the production-scale accelerator.

5 REFERENCES

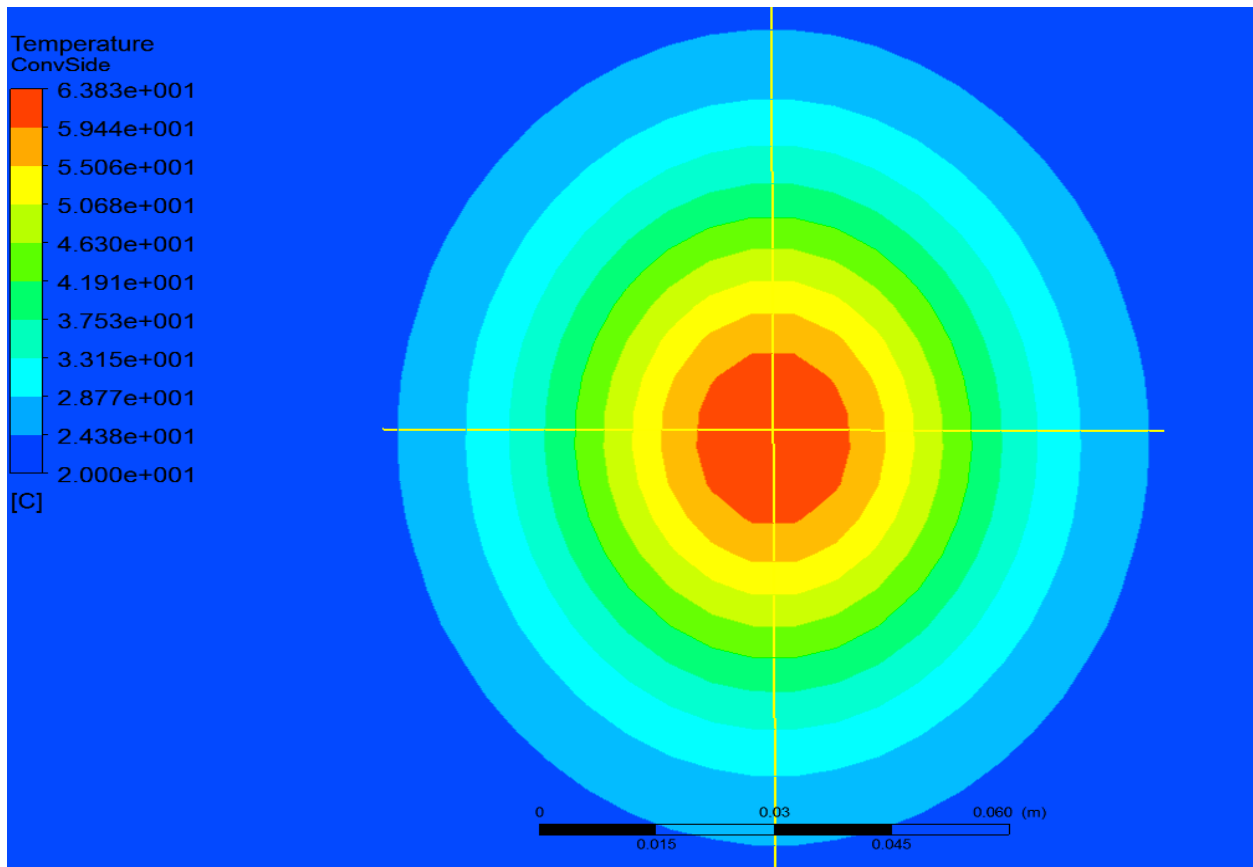
- [1] Tkac, P., S. Chemerisov, V. Makarashvili, and G.F. Vandegrift. 2011. [Development activities in support of accelerator production of Mo-99. Production through gamma/n reaction on Mo-100](http://mo99.ne.anl.gov/2011/pdfs/Mo99%202011%20Web%20Papers/S10-P4_Tkac-Paper.pdf). Molybdenum-99 Topical Meeting, Santa Fe, NM, USA, December 4–7. (http://mo99.ne.anl.gov/2011/pdfs/Mo99%202011%20Web%20Papers/S10-P4_Tkac-Paper.pdf)
- [2] Chemerisova, Sergey, George Vandegrifta, Gregory Daleb, Peter Tkaca, Roman Gromova, Vakho Makarashvilia, Bradley Micklich, Charles Jonaha, Thad Heltemesa, David Rotscha, Keith A. Woloshunb, Michael Hollowayb, Frank Romerob, and James Harveyc. 2014. [Overview of Argonne support for Mo-99 medical isotope production: NorthStar Medical Technologies](http://mo99.ne.anl.gov/2014/pdfs/papers/S8P4%20Paper%20Chemerisov.pdf). Molybdenum-99 Topical Meeting, Washington, DC, USA, June 24–27. (<http://mo99.ne.anl.gov/2014/pdfs/papers/S8P4%20Paper%20Chemerisov.pdf>)
- [3] Chemerisov, S., J. Bailey, T. Heltemes, C. Jonah, R. Gromov, V. Makarashvili, P. Tkac, D. Rotsch, M. Virgo, and G.F. Vandegrift. 2016. [Results of four one-day electron-accelerator irradiations of enriched Mo-100 targets for the production of Mo-99](http://www.ipd.anl.gov/anlpubs/2017/01/132736.pdf). Argonne technical report ANL/NE-16/26, October. (<http://www.ipd.anl.gov/anlpubs/2017/01/132736.pdf>)
- [4] Chemerisov, S., J. Bailey, T. Heltemes, C. Jonah, V. Makarashvili, P. Tkac, D. Rotsch, M. Virgo, and G.F. Vandegrift. 2016. [Results of the six-and-a-half day electron-accelerator irradiation of enriched Mo-100 targets for the production of Mo-99](http://www.ipd.anl.gov/anlpubs/2017/01/132735.pdf). Argonne technical report ANL/NE-16/27, October. (<http://www.ipd.anl.gov/anlpubs/2017/01/132735.pdf>)
- [5] Virgo, M., S. Chemerisov, R. Gromov, C. Jonah, and G.F. Vandegrift. 2016. [Results of thermal test of metallic molybdenum disk target and fast-acting valve testing](http://www.ipd.anl.gov/anlpubs/2017/01/132800.pdf). Argonne technical report ANL/NE-16/44, December. (<http://www.ipd.anl.gov/anlpubs/2017/01/132800.pdf>)
- [6] Livingood, J.J. 1969. *The Optics of Dipole Magnets*. New York: Academic Press.
- [7] Young, L.M. and J.H. Billen. 1996. “Parmela.” Los Alamos National Laboratory, LA-UR-96-1835.
- [8] RadiaBeam Technologies. (<http://www.radiabeam.com/>).
- [9] AFT Fathom (www.aft.com/products/fathom).
- [10] ANSYS (<http://www.ansys.com>).
- [11] Alford, K., S. Chemerisov, R. Gromov, L. Hafenrichter, C.D. Jonah, R. Tafoya, K. Wesolowski, D. Brown, S. Forknall, J. Gardner, D. Macrillo, and A. Zulpo. 2015. “Low Energy Accelerator Facility Upgrade and Test.” Proceedings of 12th International Topical Meeting on the Nuclear Applications of Accelerators, Washington, DC, USA, November.

This page intentionally left blank

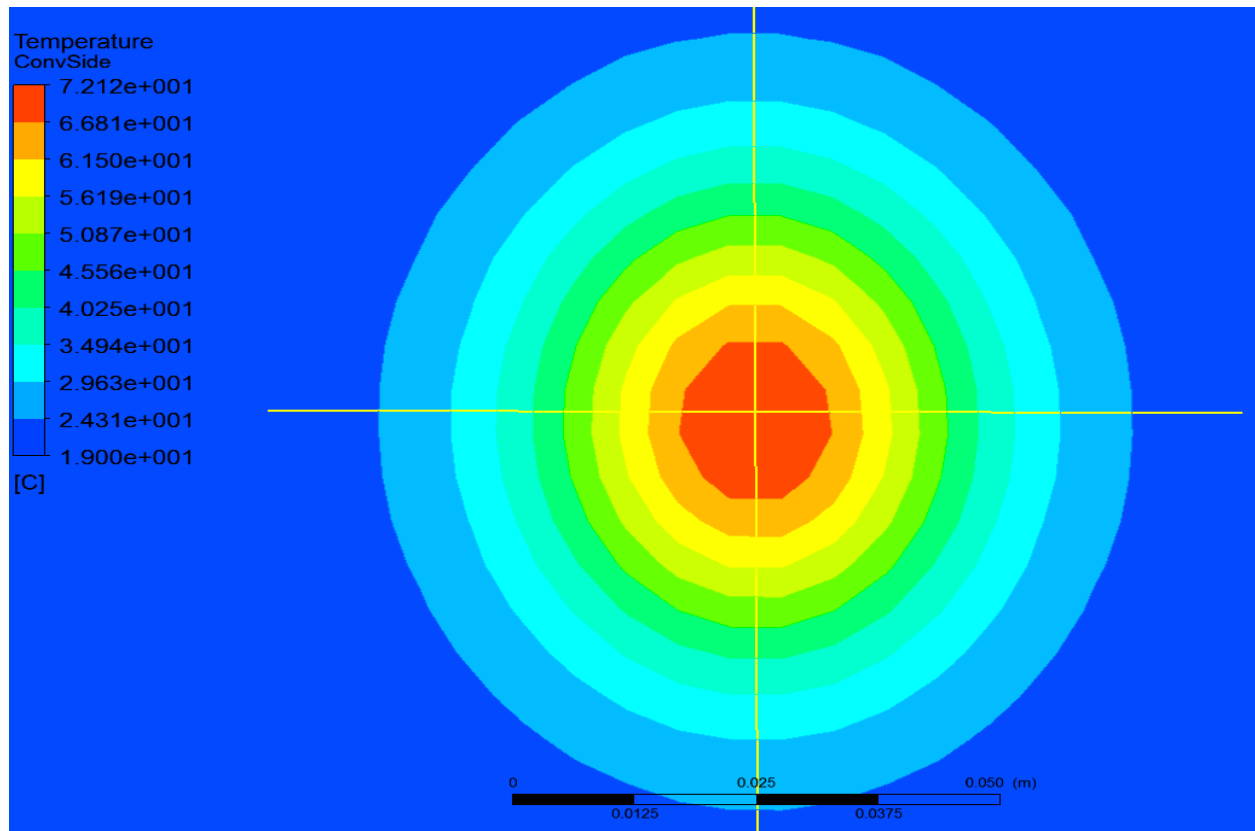
APPENDIX 1

Computer simulation of temperature distribution on the beam dump plate for different beam sizes and average beam energy. Beam supposed to be Gaussian.

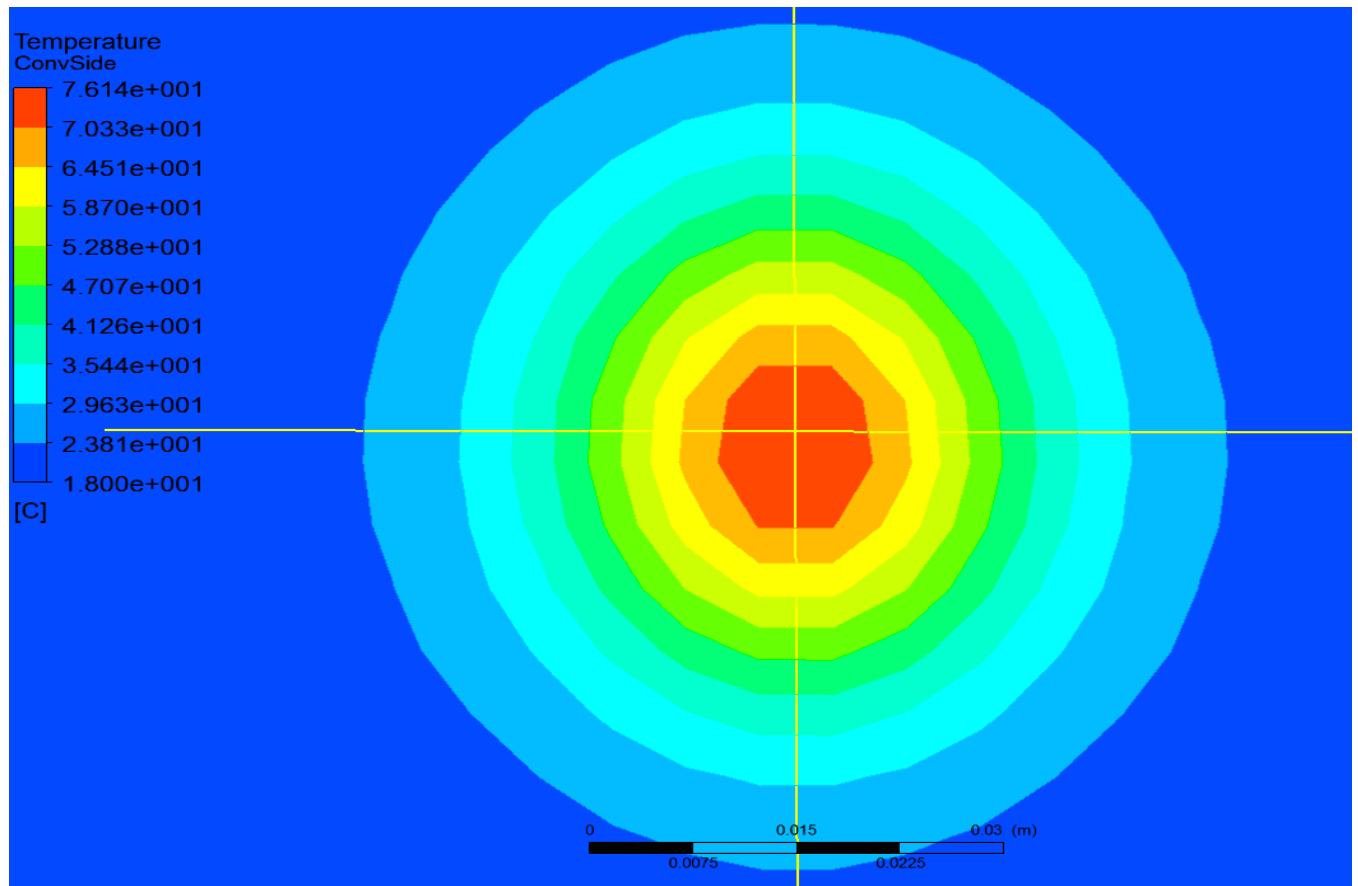
Beam 20 kW, 42 mm FWHM, 19 gpm



Beam 15 kW, 30 mm FWHM, 19 gpm



Beam 10 kW, 20 mm FWHM, 19 gpm





Nuclear Engineering Division

Argonne National Laboratory

9700 South Cass Avenue, Bldg. 208

Argonne, IL 60439-4854

www.anl.gov



Argonne National Laboratory is a U.S. Department of Energy
laboratory managed by UChicago Argonne, LLC